Angewandte Chemie International Edition
www.angewandte.org

How to cite: *Angew. Chem. Int. Ed.* **2025**, *64*, e202503037
doi.org/10.1002/anie.202503037

Solid-State Li Batteries

Electric-Dipole Coupling Ion-Dipole Engineering Induced Rational Solvation-Desolvation Behavior for Constructing Stable Solid-State Lithium Metal Batteries

*Feng Tao[+], Kaijian Yan[+], Chenxu Dong, Jiajing Wang, Qianmu Pan, Minjian Gong, Jiapei Gu, Chunli Shen, Ruohan Yu, Yuanzhi Jiang, Mingjian Yuan, Cheng Zhou, Meng Huang, Xu Xu, and Liqiang Mai**

Abstract: Solid-state polymer electrolytes (SPEs) with high ionic conductivity, a wide voltage window, and an ultrastability electrolyte/electrode interface are essential for practical applications of solid lithium-metal batteries but particularly challenging. The key to overcoming these long-term obstacles lies in the rational design of the Li^+ solvation-desolvation behavior in SPEs. Herein, we propose an electric-dipole coupling ion-dipole strategy to modulate the Li^+ solvation structure and enhance Li^+ desolvation kinetics. The experimental characterizations and theoretical calculations indicate that the free solvents and FSI^- are anchored by ion–dipole interactions, which facilitate the transfer of Li^+ and obtain a wide electrochemical stability window. Coupling the electric-dipole interactions that promote lithium salt dissociation and rapid ion desolvation contributes to obtaining more mobile Li^+ and realizing an inorganic-rich electrolyte/electrode interface. Benefiting from the above benefits, the assembled lithium symmetric cells and the full cells demonstrate ultralong cycling life. More importantly, full cells with high-loading cathodes ($LiFePO_4$ with 11.25 mg cm^{-2}, NCM811 with 7.84 mg cm^{-2}) and pouch cell still display stable cycling. This research gives valuable insights into regulating the solvation-desolvation behavior in SPEs and facilitates the development of state-of-the-art Li metal batteries.

Introduction

Lithium metal batteries (LMBs) with high energy densities have gained intensive attention.[1–3] However, the commercial application of conventional LMBs with liquid organic electrolytes faces several severe safety risks, such as the inherent flammability and leakage of liquid organic solvents.[4–6] Solid-state LMBs are recognized as promising candidates because of their high energy densities and improved security.[7–9] The key to advanced solid-state LMBs is the construction of solid-state electrolytes that have strong mechanical properties, high ionic conductivity, and flexibility.[10] Among the various solid-state electrolytes, solid polymer electrolytes (SPEs) are the most promising electrolytes for commercial LMBs due to their satisfactory elasticity and toughness to preserve optimal interface contact.[11–13]

Poly(vinylidene fluoride) (PVDF)-based SPEs have attracted extreme interest for their virtues of excellent thermal property and higher room temperature ionic conductivity compared with polyacrylonitrile or poly(ethylene oxide)-based SPEs.[14–17] It is noteworthy that during the manufacture of PVDF-based SPEs, small amounts of solvent remain in the polymer matrix even after adequate heat treatment.[18] The residual solvent interacts strongly with lithium salts to form $[Li(solvent)_x]^+$ coordination structures, which migrate along the polymer chains depending on the coordination and incoordination between electronegative fluorine (F) atoms and $[Li(solvent)_x]^+$ to achieve a high ambient temperature ionic conductivity of 1×10^{-4} S cm^{-1}.[4] Unfortunately, the existence of residual solvents in PVDF-based SPEs poses many issues.[19–21] The electrochemical instability of the residual solvents with Li metal can lead to serious interfacial side reactions, forming a solid electrolyte interphase (SEI) with poor mechanical strength, low ionic conductivity, and inhomogeneous Li^+ transport pathways, resulting in rapid dendrites growth at the electrolyte-lithium metal interface and short-circuiting of the cell.[22–25] Additionally, the poor oxidative decomposition resistance of residual solvents results in a low voltage window of the

---

[*] F. Tao[+], R. Yu, M. Huang, X. Xu
Sanya Science and Education Innovation Park of Wuhan University of Technology, Sanya 572000, P.R. China

F. Tao[+], K. Yan[+], C. Dong, J. Wang, Q. Pan, M. Gong, J. Gu, C. Shen, C. Zhou, X. Xu, L. Mai
State Key Laboratory of Advanced Technology for Materials Synthesis and Processing, School of Materials Science and Engineering, Wuhan University of Technology, Wuhan, Hubei 430070, P.R. China
E-mail: mlq518@whut.edu.cn

Y. Jiang, M. Yuan
State Key Laboratory of Advanced Chemical Power Sources, Frontiers Science Center for New Organic Matter, Key Laboratory of Advanced Energy Materials Chemistry (Ministry of Education), College of Chemistry, Nankai University, Tianjin 300071, P.R. China

X. Xu
Hubei Longzhong Laboratory, Wuhan University of Technology (Xiangyang Demonstration Zone), Xiangyang, Hubei 441000, China

[+] These authors contributed equally to this work.

Additional supporting information can be found online in the Supporting Information section

© 2025 Wiley-VCH GmbH

15213773, 2025, 21, Downloaded from https://onlinelibrary.wiley.com/doi/10.1002/anie.202503037 by WUHAN UNIVERSITY OF TECHNOLOGY, Wiley Online Library on [05/09/2025]. See the Terms and Conditions (https://onlinelibrary.wiley.com/terms-and-conditions) on Wiley Online Library for rules of use; OA articles are governed by the applicable Creative Commons License

PVDF-based SPEs and inhomogeneous cathode electrolyte interface (CEI) at high-voltage, which decreases the stability of the SPEs matching with high-voltage cathodes and leads to rapid capacity loss of the LMBs.[20,26]

Great efforts have been made to solve the aforementioned problems, including the incorporation of fillers that anchor residual solvents,[26,27] adjusting the types of lithium salt,[28] and employing additives,[29,30] etc. Among them, introducing inorganic fillers is considered a workable method to improve interfacial stability. For example, Yang et al. employed 3 Å zeolite molecular sieves as fillers for PVDF-based SPEs to anchor the residual solvent and weaken the solvent's ability to participate in the solvation of Li^+, thus modulating the solvation structure.[22] In addition, Yang and coworkers reported that $Li_{1.4}Al_{0.4}Ti_{1.6}(PO_4)_3$ nanowires were incorporated into the PVDF matrix to immobilize the free DMF, remarkably inhibiting the interfacial parasitic side reactions and improving the electrochemical performance.[23] Unfortunately, the high interfacial energy between the PVDF matrix and inorganic filler can lead to the aggregation of inorganic filler, which greatly hinders Li^+ transport, leading to unstable electrolyte/electrode interfaces.[31] Moreover, the desolvation behavior of Li^+ in SPEs is often neglected. The strong coordination capacity between the FSI^- anions and Li^+ leads to increased desolvation energy and reduces the ion conduction kinetics.[32] Consequently, it is urgent to design a novel filler to regulate the solvation structures and enhance the desolvation kinetics of Li^+ in PVDF-based SPEs to construct stabilized and compatible interfaces with both the lithium metal anode and high-voltage cathode.

In this work, an electric-dipole coupling ion-dipole strategy is proposed to modulate the Li^+ solvation structures and achieve rapid desolvation kinetics (Figure 1a). Bacterial cellulose (BC) tightly immobilizes free *N*,*N*-dimethylacetamide (DMAC) solvents and FSI^- anions through strong ion–dipole interactions, achieving modulation of the Li^+ solvation sheaths and fast ion transport kinetics. Coupling the ability of rapid Li salt dissociation and Li^+ desolvation at the interface of electrodes/electrolytes via the electric-dipole interactions of $BaTiO_3$, the prepared SPEs demonstrate a high lithium-ion transference number (0.62) and large electrochemical window (4.7 V). The solid-state lithium–lithium symmetric cells exhibit a superior cycle lifespan of over 1700 h. Solid LFP||Li batteries can stably cycle 400 cycles at 1 C with 99.5% capacity retention. The solid-state full cells with NCM811 cathode can sustain cycling of 200 times at 0.5 C. More significantly, full cells with high-loading cathodes and pouch cells demonstrate stable cycling, indicating potential commercialization applications. This work provides an effective solvation-desolvation strategy for achieving advanced solid-state LMBs.

Results and Discussion

Characteristics and Properties for Electrolytes

Initially, flexible PVDF-based electrolytes were fabricated based on the solution molding method (material synthesis, Figure S1). In the electrolyte membrane, the mass ratio of PVDF to PMMA was 3:1, and the fillers (BC and $BaTiO_3$) with different ratios (denoted as PPBC, PPBB-37, PPBB-55, PPBB-73, and PPBTO, respectively) in the total polymer (PMMA + PVDF) mass of 10 wt%. To disclose the structure features of the electrolytes, the X-ray diffraction (XRD) technique was performed (Figure 1b). The $BaTiO_3$ powder exhibits excellent purity and all diffraction peaks match perfectly with PDF#31-0174, suggesting outstanding chemical stability even when encapsulated inside the polymer matrix. The Fourier transform infrared spectroscopy (FTIR) displays a band at 1629 cm^{-1}, which indicates trapped DMAC in the matrix of polymer electrolytes (Figure 1c and Figure S2). The DMAC molecules exhibit a strong coordination ability with lithium salts to form $[Li(DMAC)_x]^+$ solvation structures, and these molecules migrate through interactions with the polymer chains of PVDF/PMMA to realize high room temperature ionic conductivity. It is clear that the peak of DMAC diminishes with the addition of BC due to the strong interaction of BC with DMAC via ion–dipole engineering, anchoring the free DMAC and therefore ensuring high ionic conductivity while reducing interfacial side reactions. To further investigate the influence of BC on the improvement of electrolyte properties and the related mechanism, the ^1H NMR spectroscopy was obtained and carefully investigated. ^1H NMR measurements exhibit that the C─H proton moved significantly toward low fields with increasing BC concentration (Figure 1d), which provides compelling evidence for the presence of various hydrogen bonding patterns and ion–dipole engineering in the hybrid electrolytes,[33,34] and guarantees the outstanding mechanical properties of the hybrid electrolytes.[35] Furthermore, the existing hydrogen bonding forces between the BC and PVDF/PMMA chains contribute to the composite polymer framework stability. The thickness of the PPBB-55 electrolyte is around 93.6 µm, and other electrolytes have similar thicknesses (Figure 1e and Figure S3). The hybrid electrolytes show a more compact structure and the microstructure size of PVDF decreased obviously with the increasing content of BC, which may be due to that the BC provides more hydrogen bonding with the polymer matrix through ion–dipole engineering (Figure 1f and Figure S4). The corresponding energy dispersive spectroscopy (EDS) elemental maps display that the BC and $BaTiO_3$ are evenly distributed in the PVDF/PMMA matrix (Figure 1g and Figure S4).

To explore the optimal proportion between BC and $BaTiO_3$, the ionic conductivities at different temperatures and Li^+ transference numbers (t_{Li^+}) of electrolytes were measured. The ion conductivity calculated by the results of electro-chemical impedance spectroscopy (EIS) all show a tendency to increase with temperature (Figure 2a and Figure S5), which is due to the fact that an elevated temperature promotes chain movement in the polymer matrix. The conductivity gradually decreased with the addition of BC may be ascribed to the excellent encapsulation ability of ion–dipole engineering restricting the transport of free anions, which agrees with previous reported studies (Figure 2b).[36,37] But PPBB-55 still exhibits a high conductivity (3.44×10^{-4} S cm^{-1}) at 25 °C, which is superior to previously published PVDF-based electrolytes (Table S1). In

© 2025 Wiley-VCH GmbH

15213773, 2025, 21, Downloaded from https://onlinelibrary.wiley.com/doi/10.1002/anie.202503037 by WUHAN UNIVERSITY OF TECHNOLOGY, Wiley Online Library on [05/09/2025]. See the Terms and Conditions (https://onlinelibrary.wiley.com/terms-and-conditions) on Wiley Online Library for rules of use; OA articles are governed by the applicable Creative Commons License

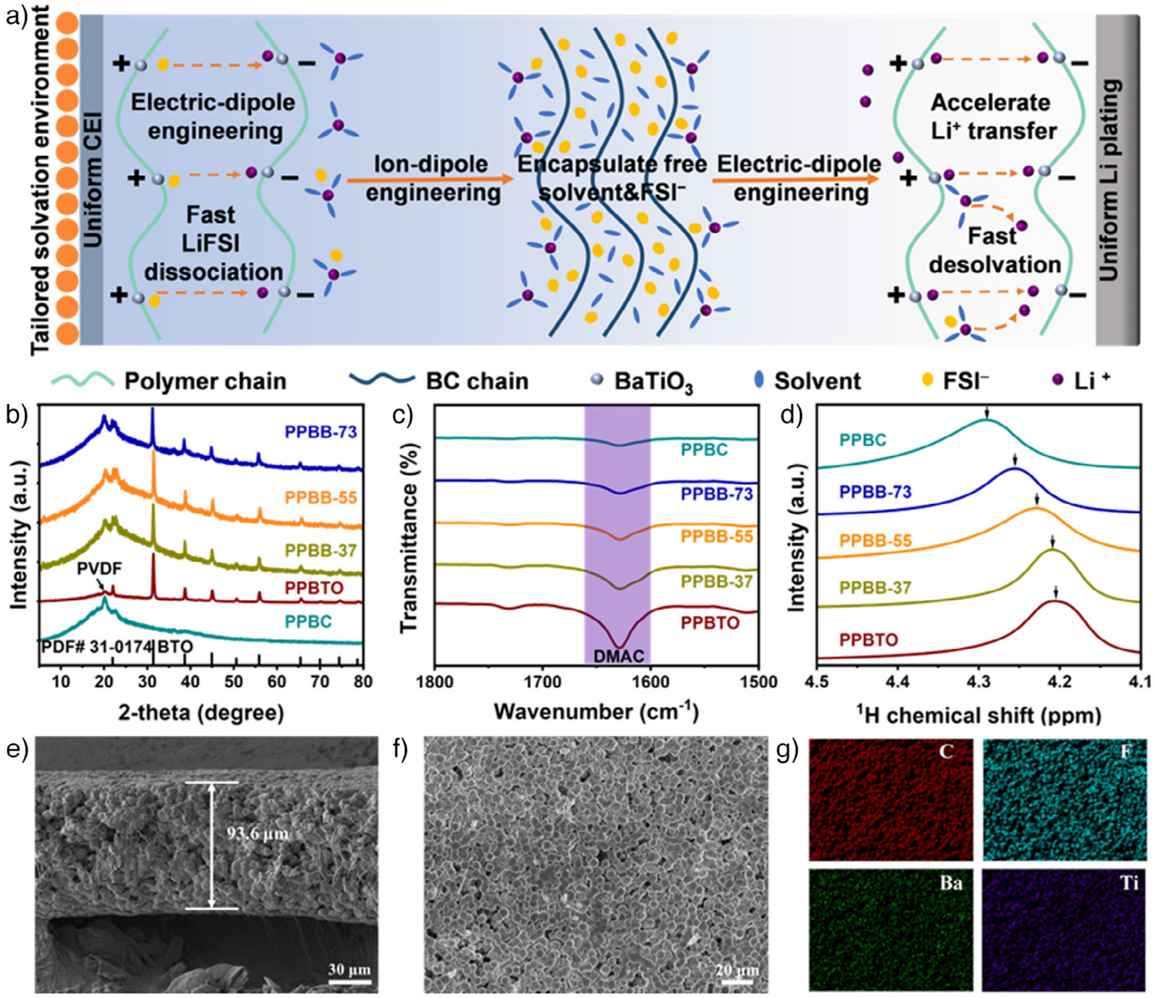

Figure 1. a) Schematic illustration of the electric-dipole coupling ion–dipole engineering mode in PPBB electrolyte. b) XRD patterns, c) FTIR spectra at the wavenumbers of 1800–1500 cm^{-1}, and d) ^{1}H NMR of hybrid electrolytes. The SEM images of cross-section e) and surface f) for the PPBB-55 electrolyte membrane and g) the corresponding EDS elemental mappings.

addition, the temperature-dependent ionic conductivities fit very consistent with the Arrhenius behavior. The activation energy (E_a) of PPBB-55 was calculated to be 0.116 eV, indicating the facilitation of Li ion migration (Figure 2c). A high t_{Li^+} is a pivotal indicator of Li$^+$ migration in hybrid electrolytes and the key to achieving high-rate performance in full cells. According to the Bruce–Vincent–Evans method, the PPBB-55 has much higher t_{Li^+} (0.62) than PPBTO (0.24), PPBB-37 (0.44), PPBB-73 (0.41), and PPBC (0.18; Figure 2d,e and Figure S6), and also higher than other reported SPEs (Table S1). Based on the aforementioned results, PPBB-55 was used in the following studies (denote as PPBB).

The coordination environment of FSI$^-$ anion in hybrid electrolytes was first studied through Raman spectroscopy. The Raman scattering peaks at 722, 740, and 743 cm^{-1} derive from a free FSI$^-$ anion, a contact-ion pair (CIP, one FSI$^-$ anion coordinated with one Li ion), and aggregate clusters (AGGs, one FSI$^-$ anion coordinated to two or more Li ions), respectively. From Figure S8, the free FSI$^-$, CIP and AGGs contents in the PPBTO electrolyte are 12.33%, 46.95%, and 40.72% (Figure S8a,c), respectively, and the corresponding contents for the PPBC electrolyte are 8%, 46.49%, and 45.29% (Figure S8b,d), respectively. The value of free FSI$^-$ in PPBB is 18.48%, significantly higher than PPBC and PPBTO (Figure 2f and Figure S7).

The above experimental results demonstrate that BaTiO$_3$ plays a primary contribution in lithium salt dissociation via its electric-dipole engineering and BC plays a secondary role. Figure S9 displays a schematic illustration of the electric-dipole engineering constructed from BaTiO$_3$ through density functional theory (DFT) calculations. When an applied electric field is provided, electrons move from Ti atoms to O atoms and an electron cloud is formed around the O atoms, thus inducing the formation of the electric dipole. As has been established by previous theoretical and experimental results, the electric-dipole can greatly facilitate the LiFSI dissociation and the rapid Li$^+$ desolvation, resulting in the generation of more mobile Li$^+$.[14,38,39] Consequently, the ion-dipole engineering of BC restricts the free anion migration, while the electric dipole engineering of BaTiO$_3$ promotes the dissociation of LiFSI and the rapid ion desolvation, and the coupling of the two engineering can achieve a high t_{Li^+} for PPBB.

© 2025 Wiley-VCH GmbH

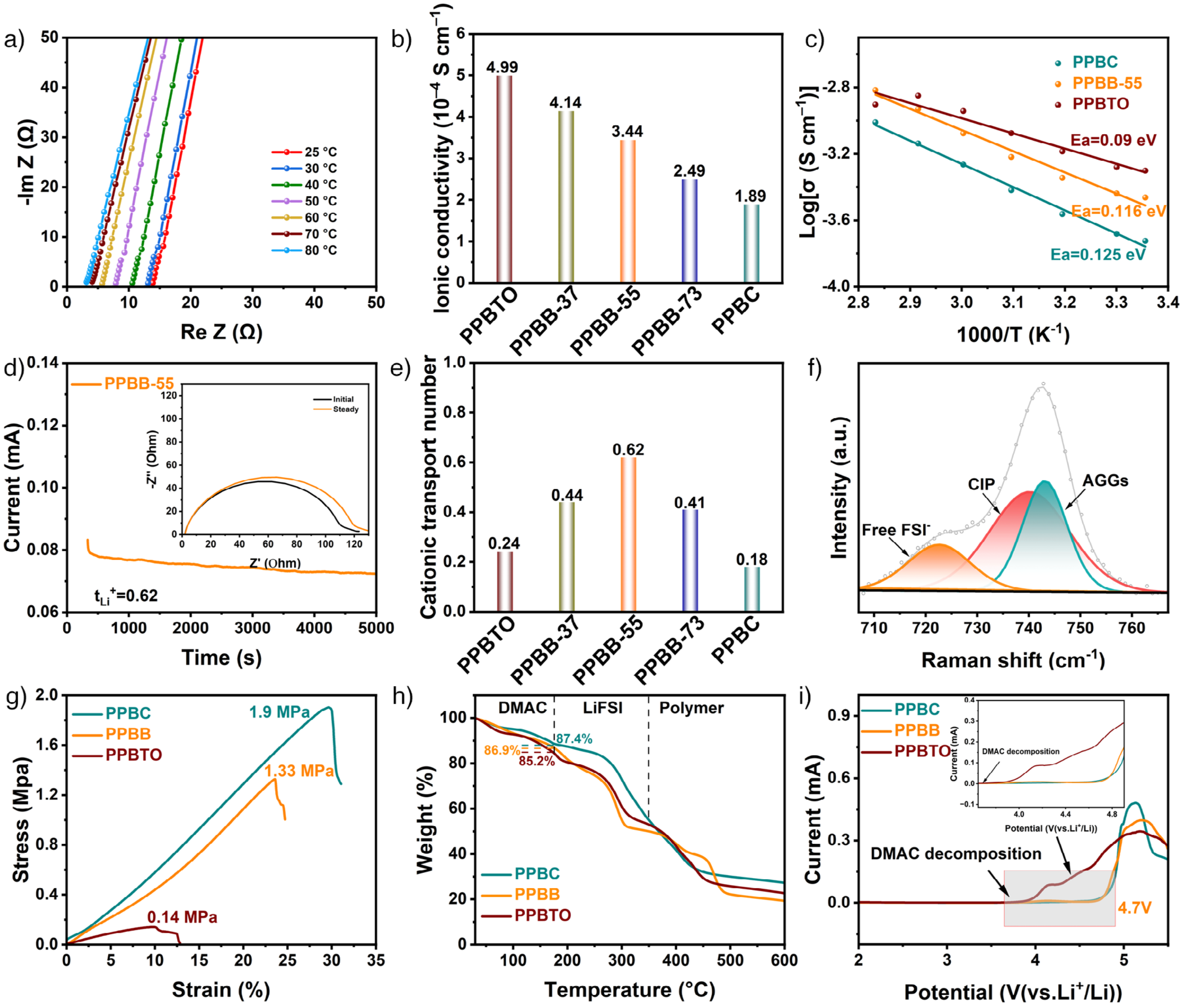

Figure 2. Characterization of the lithium salt dissociation and Li^+ transfer properties. a) EIS of SS|PPBB-55|SS batteries at different temperatures and b) ionic conductivities of hybrid electrolytes with 25 °C. c) Arrhenius plots and calculated activation energy of PPBC, PPBTO, and PPBB-55 electrolytes. d) The current-time curve for Li|PPBB-55|Li battery (The before and after polarization of the battery EIS displayed in the inset). e) Lithium transference number of hybrid electrolytes. f) Raman spectra of the PPBB electrolyte. g) Stress–strain curves, h) TGA curves and i) LSV curves of PPBC, PPBTO, and PPBB electrolytes.

Besides the ionic transfer feature of SPEs, the mechanical characteristics are also critical toward the interface contact and stability. The tensile value considerably improved from 0.14 MPa for PPBTO to 1.9 MPa for PPBC (Figure 2g), which may be due to the more hydrogen bond generation through ion–dipole engineering between BC and the polymer matrix. The increased mechanical properties can effectively inhibit the rapid growth of lithium dendrites and relieve the volume changes of the lithium metal anode during operation. Thermogravimetry analysis (TGA) results reveal the presence of residual DMAC solvent in PPBC, PPBTO, and PPBB electrolytes, which agree with the results from FTIR (Figure 2h). The residual DMAC contents in PPBTO, PPBB, and PPBC below the test temperature of 175 °C (slightly above the boiling point of DMAC, which is 165.1 °C) are determined to be 14.8, 13.1, and 12.6 wt%, respectively. Notably, the small difference in the content of DMAC among these electrolytes suggests that the enhanced conductivity observed in PPBTO is not primarily influenced by DMAC content. The small amount of DMAC in the hybrid electrolytes contributes to the migration of Li ions, resulting in large ionic conductivity. Nevertheless, the continuous decomposition of DMAC at high potential results in a low voltage stability window for the electrolytes. Generally, the residual DMAC decreases the compatibility of hybrid electrolytes with high-voltage cathodes, resulting in worse cycle performance of the cells. As illustrated in Figure 2i, the linear sweep voltammetry (LSV) results indicate that PPBB and PPBC can work up to 4.7 V, higher than that of PPBTO (3.9 V). This high electrochemical stability window may be attributed to the ion–dipole engineering of BC, which can tightly anchor the free DMAC and hinder the DMAC molecules decomposition

© 2025 Wiley-VCH GmbH

15213773, 2025, 21, Downloaded from https://onlinelibrary.wiley.com/doi/10.1002/anie.202503037 by WUHAN UNIVERSITY OF TECHNOLOGY, Wiley Online Library on [05/09/2025]. See the Terms and Conditions (https://onlinelibrary.wiley.com/terms-and-conditions) on Wiley Online Library for rules of use; OA articles are governed by the applicable Creative Commons License

15213773, 2025, 21, Downloaded from https://onlinelibrary.wiley.com/doi/10.1002/anie.202503037 by WUHAN UNIVERSITY OF TECHNOLOGY, Wiley Online Library on [05/09/2025]. See the Terms and Conditions (https://onlinelibrary.wiley.com/terms-and-conditions) on Wiley Online Library for rules of use; OA articles are governed by the applicable Creative Commons License

at high voltage. Differential scanning calorimetry (DSC) analysis reveals that the glass transition temperature (T_g) for PPBTO, PPBB, and PPBC is determined to be 103.3, 105.4, and 113.5 °C, respectively (Figure S10). The relatively slightly higher T_g value of PPBB is due to the stiff BC limiting the movement of the polymer chain segments,[36,37] but its ion–dipole coupled electric-dipole effect enables it to achieve a high Li^+ transfer number.

Compatibility Assessment with Lithium Anode

The symmetric lithium cells were cycled to assess the performance of the PPBB electrolyte. As a key indicator of electrolyte-lithium metal interfacial stability and lithium dendrite growth, the critical current density (CCD) of Li|PPBB|Li cell with 0.9 mA cm^{-2} (Figure 3a), which is significantly larger than that of the lithium symmetric cells with PPBC electrolyte (0.7 mA cm^{-2}) and PPBTO electrolyte (0.3 mA cm^{-2}), which suggests that the ability to inhibit lithium dendrites is enhanced. Subsequently, the ion diffusion kinetics across the electrode/electrolyte interface were assessed using the Tafel polarization curve. The exchange current density values (j_0, Figure 3b) derived from the intercepts indicate that j_0 for the symmetric cell with PPBB electrolyte (0.16 mA cm^{-2}) is much larger than that of the symmetric cells with PPBC (0.04 mA cm^{-2}) and PPBTO electrolytes (0.13 mA cm^{-2}). The experiment of one-sided plating lithium illustrated in Figure 3c further visualizes that the PPBB electrolyte can significantly prolong the time necessary for dendrites lithium to puncture the SPEs at 0.1 mA cm^{-2}. To further assess the practicability of PPBB on stabilizing the interface with Li metal, the lithium symmetric batteries were assembled with PPBB, PPBC, and PPBTO electrolytes. Initially, the symmetric cells were measured under a constant current density of 0.1 mA cm^{-2} at ambient temperature. From Figure 3d, the PPBB electrolyte presents a stable cycle life of over 1700 h with a low polarization (27 mV), while the Li|PPBTO|Li and Li|PPBC|Li symmetric cells fail after 200 and 900 h, respectively. In addition, the Li||Li symmetric cell with PPBB electrolyte can stably operate for 300 h with an overpotential of 67 mV under 0.25 mA cm^{-2} with 0.25 mAh cm^{-2}. In sharp contrast, PPBTO and PPBC electrolytes exhibit a much shorter cycling lifespan of 72 and 120 h, respectively (Figure 3e). Compared to previously reported solid-state PVDF-based batteries, the results in our work show state-of-the-art cycling stability (Table S2). SEM was conducted to assess the surface morphology of lithium metal after Li||Li symmetrical cells cycling. As displayed in Figure 3f,h, a quite rough Li foil surface with apparent dendritic lithium for the PPBTO (Figure 3f) and PPBC (Figure 3h) electrolytes is observed. By comparison, the cycled Li metal using the PPBB electrolyte exhibited a much flatter and more uniform morphology (Figure 3g).

To obtain a profound insight into the influence of PPBB electrolyte on Li deposition behavior, time-of-flight secondary ion mass spectrometry (ToF-SIMS) 3D rendering models and their corresponding depth profiles (Figure 3i) were performed to identify the chemical compositions of SEI. It can be seen that inorganic-rich species are observed in the SEI. Particularly, the signal of LiF^- dominates the SEI composition. The presence of inorganic-rich species not only enhances the mechanical properties of the SEI layer but also benefits the uniform Li^+ deposition and inhibits the lithium dendrites propagation. Based on them, the SEI structure of Li||Li symmetrical cell with PPBB electrolyte was constructed in Figure 3j, which plays a prominent role in suppressing interfacial parasitism side reactions and lithium dendrite growth.

Research on the Effect Mechanism of PPBB Electrolyte

To further understand the influence of filler on electrolyte/lithium anode interfacial stability, the X-ray photoelectron spectra (XPS) and ToF-SIMS techniques were employed to compare the components of SEI on the cycled lithium anode surface with different electrolytes. From the XPS results, the SEI primarily consists of inorganic species and C-containing organic species (Figure 4a–c), which comes from the decomposition of DMAC solvents, polymer matrix and FSI^-.[22] In Figure 4a, the C=O is detected on the lithium foil surface from the C 1 s spectra, which is mainly ascribed to the decomposition of DMAC solvent. The PPBB and PPBC electrolytes have less C=O, which suggests that the decomposition of DMAC is greatly suppressed.[22,23] The peak of LiF is observed at the F 1 s spectrum (Figure 4b), which is the decomposition product of FSI^-.[22] Fewer LiF indicate that the BC in PPBB and PPBC electrolytes can tightly anchor the FSI^- anions, which facilitates the transfer of Li^+.[40,41] As displayed in Figure 4c, the peak intensity of N−C=O derived from DMAC decomposition decreases with the increased BC concentration at the N 1 s spectrum. This result can be attributed to the immobilization of free DMAC by BC, thus improving the voltage window of the PPBC electrolyte.[23,42] These observations can also be validated by ToF-SIMS (Figure 4d and Figure S11). The LiF^- and C_2HO^- anions represent inorganic LiF and organic compounds, respectively. More LiF^- and C_2HO^- anions demonstrate more free FSI^- and DMAC decomposition. The above analyses of the cycled Li foils evidence that the introduction of BC can immobilize free FSI^- anions and DMAC through ion–dipole engineering, therefore adjusting the coordination environment of Li^+ to achieve a highly robust electrolyte/electrode interfacial.

To further disclose the function of BC on the Li^+ solvation-desolvation behavior in electrolytes, molecular dynamics (MD) simulation and DFT calculations were carried out. The adsorption energy of BC to DMAC molecules is −1.52 eV higher than $BaTiO_3$ to DMAC (−0.86 eV, Figure 4e and Figure S12a). In addition, the high adsorption energy verifies the strong adsorption effect of BC on FSI^- anion (Figure 4f and Figure S12b). The high binding energy between BC and DMAC may be due to the strong adsorption of DMAC by the OH^- on BC (−0.86 eV, Figure S12c). DFT calculations are consistent with XPS and ToF-SIMS results, demonstrating the strong anchoring effect of BC on free FSI^- and DMAC, which facilitates Li ion transport and increases the electrochemical stability window. Furthermore, MD

© 2025 Wiley-VCH GmbH

15213773, 2025, 21, Downloaded from https://onlinelibrary.wiley.com/doi/10.1002/anie.202503037 by WUHAN UNIVERSITY OF TECHNOLOGY, Wiley Online Library on [05/09/2025]. See the Terms and Conditions (https://onlinelibrary.wiley.com/terms-and-conditions) on Wiley Online Library for rules of use; OA articles are governed by the applicable Creative Commons License

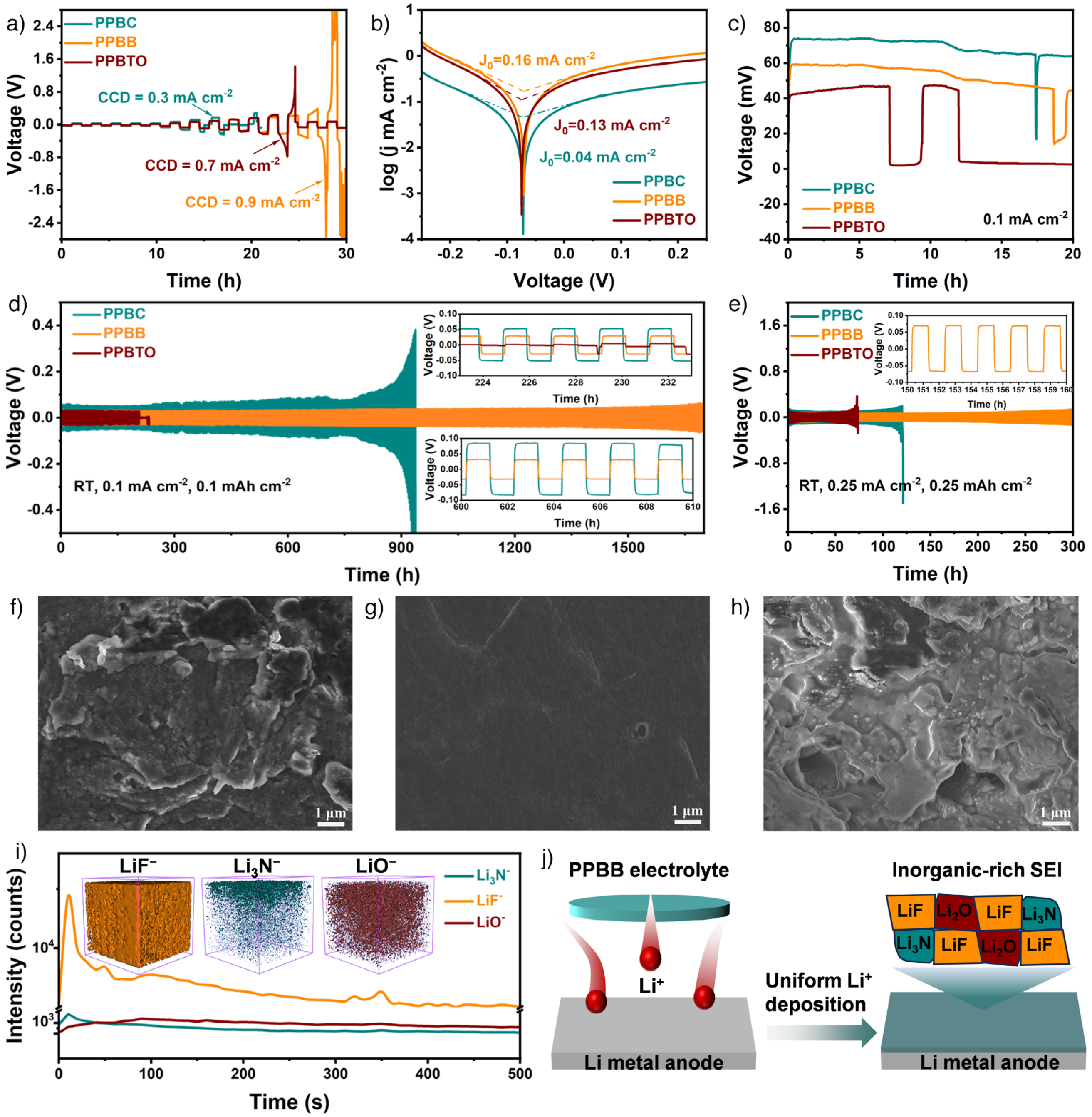

Figure 3. The performance of Li|electrolytes|Li batteries. a) Critical current density; b) tafel plots; c) galvanostatic charging tests under 0.1 mA cm^{-2}; cycling performance at d) 0.1 mA cm^{-2} with 0.1 mA h cm^{-2}, and e) 0.25 mA cm^{-2} with 0.25 mA h cm^{-2}. SEM images of cycled lithium metal disassembled from Li|electrolytes|Li cells. f) PPBTO; g) PPBB; and h) PPBC. i) ToF-SIMS depth profiles and 3D distribution schematic diagram (inset) of the lithium electrodes after 50 cycles with PPBB electrolyte. j) Schematic representation of the components of the SEI layer generated at the PPBB electrolyte/lithium anode interface.

simulations were performed to further explore the influence of BC on the solvation structures of Li$^+$ (Figure 4g and Figure S13). The radial distribution function (RDF) demonstrates that BC is involved in the construction of the Li$^+$ solvation structures (Figure 4h and Figure S14). Additionally, the typical solvation clusters in different electrolytes were obtained from MD simulations (Figure 4j and Figure S15). The solvated cluster of Li(1)DMAC(4) (Figure S16) emerges as a predominant solvated structure, which accounts for a lower percentage of the electrolyte with BC (35%) than that of the electrolyte without BC (42%), demonstrating that BC promotes lithium ion desolvation to some extent. The solvation sheath of Li involved with BC is about 1%, and the corresponding typical structures are shown in Figure 4i. The above results suggest that BC alters and participates in the Lithium ions solvation structure through ion–dipole

© 2025 Wiley-VCH GmbH

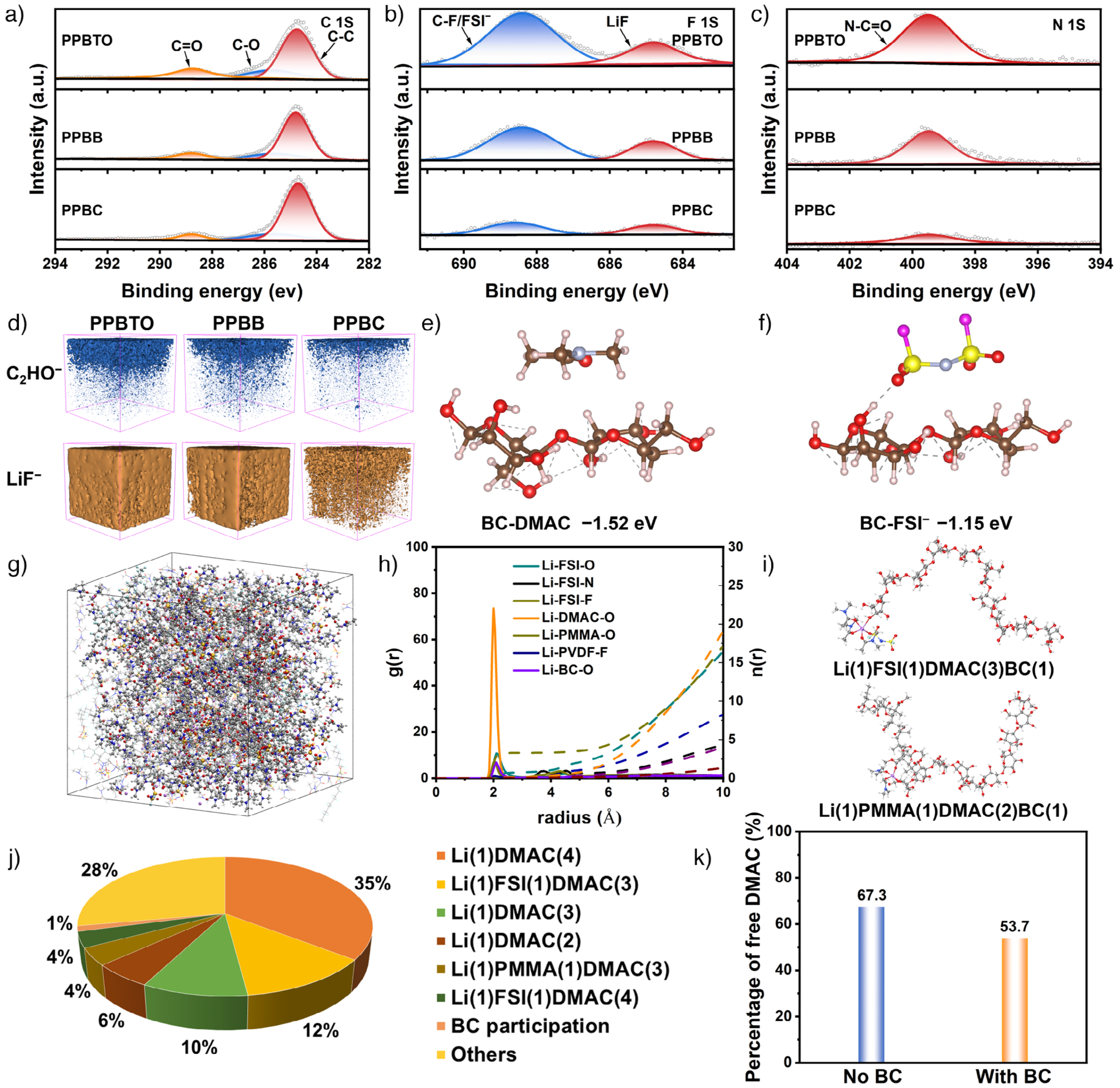

Figure 4. Mechanism of electric-dipole coupling ion–dipole engineering. High-resolution XPS spectrum of a) C 1 s, b) F 1 s, and c) N 1 s for lithium anode surface in Li|electrolytes|Li after 50 cycles. d) ToF-SIMS 3D distribution schematic diagram of the lithium electrodes after 50 cycles with different electrolytes. e) Adsorption energy of BC with DMAC. f) Adsorption energy of BC with FSI^-. g) MD simulation snapshots and h) RDF results of the electrolytes with BC. i) Typical solvation structures of BC involved. j) Statistically coordinated species distribution of electrolyte with BC. k) Percentage of free DMAC in electrolytes with BC and without BC.

engineering. Furthermore, it can be seen that the percentage of free DMAC solvent molecules decreases from 67.3% for the electrolyte without BC to 53.7% for the electrolyte with BC in Figure 4k. This difference further indicates that the addition of BC increases the anchoring of DMAC solvent molecules, thus alleviating the interface side reactions caused by free solvent molecules and increasing the electrochemical stability window.

Full Cell Performance

To further demonstrate the effects of Li^+ solvation structure regulation and desolvation kinetics improvement on electrochemical performance, the full batteries with LFP and NCM811 cathodes were constructed and evaluated. The cyclic voltammetry (CV) results reveal that the LFP|PPBB|Li cell (Figure S17b) shows much better redox reaction stability

© 2025 Wiley-VCH GmbH

15213773, 2025, 21, Downloaded from https://onlinelibrary.wiley.com/doi/10.1002/anie.202503037 by WUHAN UNIVERSITY OF TECHNOLOGY, Wiley Online Library on [05/09/2025]. See the Terms and Conditions (https://onlinelibrary.wiley.com/terms-and-conditions) on Wiley Online Library for rules of use; OA articles are governed by the applicable Creative Commons License

15213773, 2025, 21, Downloaded from https://onlinelibrary.wiley.com/doi/10.1002/anie.202503037 by WUHAN UNIVERSITY OF TECHNOLOGY, Wiley Online Library on [05/09/2025]. See the Terms and Conditions (https://onlinelibrary.wiley.com/terms-and-conditions) on Wiley Online Library for rules of use; OA articles are governed by the applicable Creative Commons License

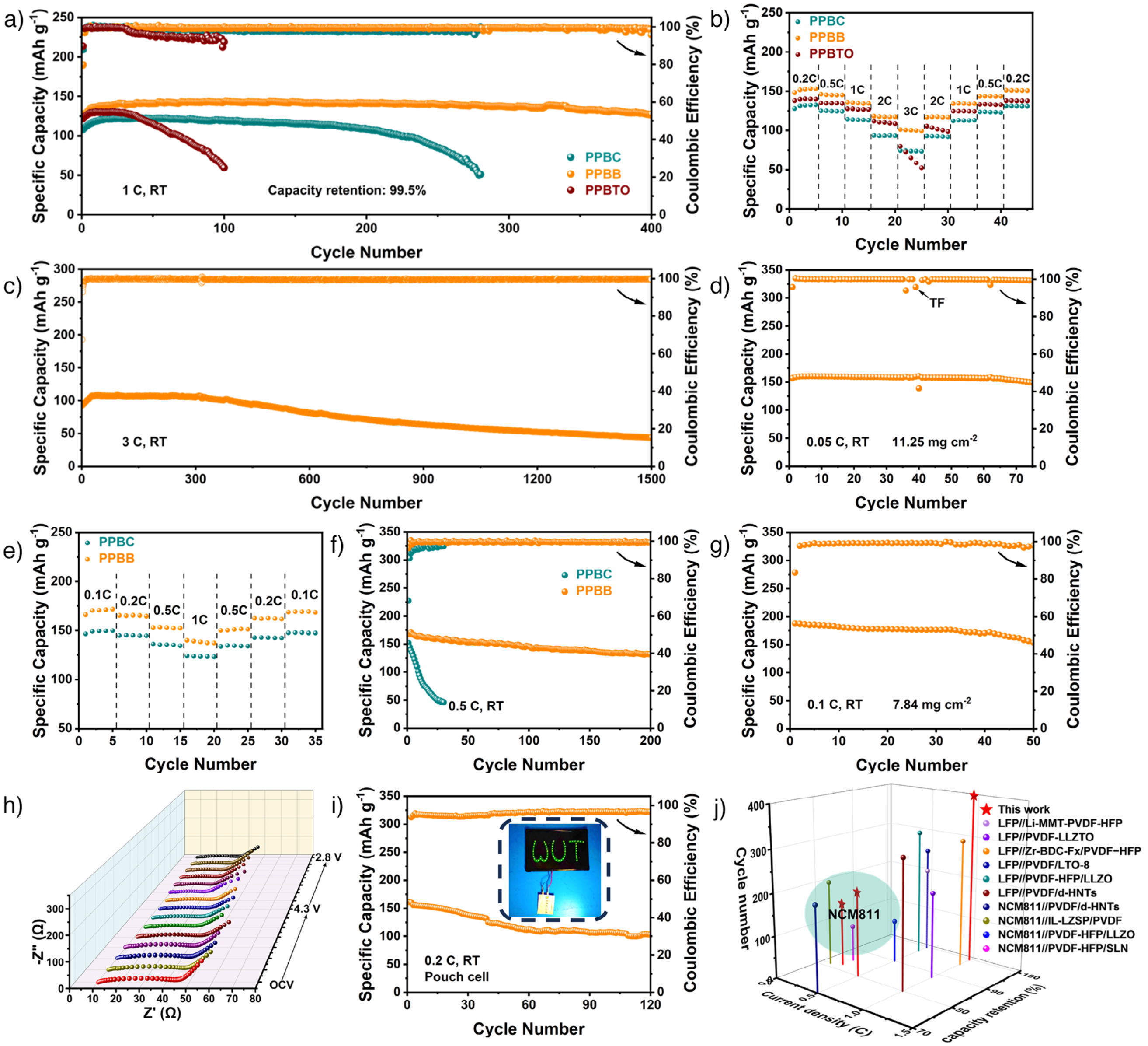

Figure 5. Cycling stability of the full batteries at RT. Long-term cycling stability of Li||LFP batteries at a) 1 C and c) 3 C. b) Rate capacities of Li||LFP cells employing various electrolytes. d) Cycling stability of LFP||Li at a cathode loading of 11.25 mg cm^{-2}. Temperature fluctuation (TF) and thermal insulation systems failed. e) Rate capacities of NCM811||Li cells with various electrolytes. f) Cycling performance of Li||NCM811 batteries at 0.5 C. g) Electrochemical performance of Li||NCM811 cell with a high cathode loading of 7.84 mg cm^{-2}. h) Nyquist plots of the Li||NCM811 cell using PPBB electrolyte obtained from the in-situ EIS test. i) Cycling performance of solid-state Li||LFP pouch battery at 0.2 C. Inset: Optical picture of solid-state LFP||Li pouch cell powering an LED. j) Comparison of full batteries performance of recently reported PVDF-based SPEs.

and reversibility than the LFP|PPBTO|Li (Figure S17a) and LFP|PPBC|Li (Figure S17c) cells during four cycles, demonstrating that interfaces formed between the PPBB electrolyte and LFP cathode are more stable. Therefore, the LFP|PPBB|Li cells deliver most outstanding electrochemical performance. In particular, at the rate of 0.2, 0.5, 1, 2, and 3 C, the capacities of the LFP|PPBB|Li battery are 153.2, 145.1, 134.6, 117.2, and 99.4 mAh g^{-1}, respectively (Figure 5b), especially at 3 C, much better than LFP|PPBC|Li battery (73.4 mAh g^{-1} at 3 C) and LFP|PPBTO|Li cell (79.8 mAh g^{-1} at 3 C). The LFP|PPBTO|Li battery at 3 C with dramatic capacity decrease may be due to its inferior mechanical properties. The charging/discharging plateaus of the LFP|PPBB|Li battery widened slightly and remained stable as the currents increased (Figure S18b). Nevertheless, the overpotential of LFP|PPBC|Li battery (320 mV, Figure S18c) and LFP|PPBTO|Li battery (171 mV, Figure S18a) expands remarkably with the increase of current, suggesting high lithium ion transfer resistance. The interface impedance of the pristine LFP|PPBB|Li cell is low and increases slightly after the rate test (Figure S19). By comparison, the resistance of the LFP|PPBC|Li battery and the LFP|PPBTO|Li battery increased dramatically after the rate test (Figure S19). Owing to the excellent Li^{+} transport performance of the PPBB, the

© 2025 Wiley-VCH GmbH

assembled LFP|PPBB|Li cells exhibit consistently remarkable cycle stabilization of 400 cycles at 1 C with a high-capacity retention of 99.5% (Figure 5a). By sharp contrast, the LFP||Li batteries with PPBTO and PPBC electrolytes demonstrate rapid capacity degradation under the same conditions. Furthermore, the LFP|PPBB|Li battery can stably operate for 1500 cycles under 3 C (Figure 5c). Even with a high LFP loading of 11.25 mg cm^{-2}, the LFP|PPBB|Li battery exhibits a discharge capacity of 156.8 mAh g^{-2} at 0.05 C and achieves a capacity decay of only 5% after 75 cycles (Figure 5d).

Additionally, the PPBB and PPBC electrolytes with an extending electrochemical window of 4.7 V can be compatible with the NCM811 cathode. The CV measurements indicate that the NCM811||Li cells with PPBB electrolyte (Figure S20a) have considerably improved redox dynamics compared to with the PPBC electrolyte (Figure S20b), which indicates a favorable interfacial property of the PPBB electrolyte with the NCM811 cathode. Because of the higher t_{Li^+} of PPBB electrolyte, at the current densities of 0.1, 0.2, 0.5, and 1 C, the NCM811|PPBB|Li cell reveals outstanding discharge specific capacities of 171.7, 164.6, 152.4, and 137.1 mAh g^{-1}, respectively (Figure 5e). Moreover, after the rate returns to 0.1 C, the discharge capacity recovers to 168.4 mAh g^{-1}, demonstrating an excellent rate recoverable ability. As displayed in Figure S21, the charge/discharge curves indicated that the NCM811|PPBB|Li cells (Figure S21a) have lower polarized (410 mV) compared to the NCM811|PPBC|Li cells (600 mV, Figure S21b), which suggests superior interfacial stability between the NCM811 electrodes and PPBB. The long-cycle stability of NCM811||Li batteries under various current densities was examined to assess the practicability of the PPBB electrolyte. The NCM811|PPBB|Li cells demonstrate stable cycling at a small current density of 0.2 C (Figure S22). The discharge-specific capacity can remain at 139.2 mAh g^{-1} after 150 cycles with a retention of 82.1%. In sharp contrast, after 150 cycles, the NCM811|PPBC|Li batteries display significant capacity degradation, showing only 7.9% capacity retention. At a higher rate density of 0.5 C, the NCM811|PPBB|Li cells still demonstrated excellent stability, delivering a capacity of 131.7 mAh g^{-1} with a capacity retention of 80% after 200 cycles (Figure 5f). In sharp comparison, the NCM811|PPBC|Li cell capacity decays to 0 mAh g^{-1} in less than 50 cycles. More importantly, under high NCM811 loading with 7.84 mg cm^{-2}, NCM811|PPBB|Li cell can sustain a cycle for 50 cycles at the current density of 0.1 C (Figure 5g). These outcomes are consistent with the information exhibited by the in-situ EIS (Figure 5h and Figure S23). The interface impedance evolution of NCM811|PPBB|Li cells in the in-situ EIS test is much lower and more stable compared to NCM811|PPBC|Li cells during charging and discharging. This suggests that a more compatible interfacial contact is formed between the electrodes and the PPBB electrolyte. Moreover, a flexible pouch cell was constructed further to assess the commercialization potential of the PPBB electrolyte. At 0.2 C and room temperature, the LFP|PPBB|Li pouch cell delivers a discharge capacity of 161 mAh g^{-1} with 64% retention after 120 cycles (Figure 5i). In addition, the solid-state LFP|PPBB|Li pouch cell can effectively make the light-emitting diodes (LEDs) brighten, demonstrating the practical application feasibility of PPBB electrolyte (Figure 5i). The above outcomes indicate that the PPBB electrolyte exhibits excellent cycling performance compared to the recently reported PVDF-based electrolyte works in Figure 5j and Table S3.

Interfacial Stability of PPBB with NCM811 Cathode and Li Anode

The composition of CEI is critical for the stability of the cathode/electrolyte interfacial. The CEI formation was characterized by high-resolution transmission electron microscope (HR-TEM). As illustrated in Figure 6a, a uniform amorphous (CEI) layer is observed on the top side of the cycled NCM811 cathode with PPBB electrolyte, which is due to the fast Li$^+$ desolvation promoted by the electric-dipole engineering. In sharp contrast, in the PPBC electrolyte, the CEI layer is thicker and nonuniform due to the extremely slow Li$^+$ desolvation kinetics resulting in slow Li$^+$ transport via the CEI and thus a higher cathode-electrolyte interfacial resistance (Figure 6b). The XPS tests was carried out to investigate the CEI components. As displayed in the F 1 s high-resolution spectra (Figure 6c,d), the CEI layer using PPBB electrolyte has more LiF content, suggesting the CEI layer is more stable, which mitigates the cathode particle decomposition and improves the cycling stability. In the C 1 s high-resolution spectra (Figure S24), the C=O peaks originate from the oxidation of N−C=O in DMAC. The lower intensity of the C=O peaks when using the PPBC electrolyte (Figure S24b) suggests that the decomposition of DMAC is greatly inhibited by ion–dipole engineering.[23] Additionally, to further verify more LiF on the surface of cycled NCM811 cathode with PPBB electrolyte, the ToF-SIMS measurements were employed. The 3D reconstruction images reveal the distribution of LiF in the CEI, which is represented by the signal of $\mathrm{LiF_2^-}$ anions (Figure 6e,f). The higher LiF content of CEI in the cycled NCM811|PPBB|Li cells is consistent with the findings of the XPS (Figure 6g). Furthermore, the $\mathrm{C_2HO^-}$ anion represents the organic component of the CEI primarily from the decomposition of DMAC (Figure S25). From the 3D reconstruction images of $\mathrm{C_2HO^-}$ and overlay (Figures S26, S27), both electrolytes exhibit low contents. The lower $\mathrm{C_2HO^-}$ content when using PPBC electrolyte suggests that free DMAC is anchored by BC through its ion-dipole engineering. The above results indicate that a LiF-rich CEI layer is established on the cycled NCM811 cathode/PPBB electrolyte interface (Figure 6h).

In addition, the lithium foil surface microstructure in the cycled full cells with NCM811 cathode was also detected. From the SEM images, a considerable rough surface is found on Li foil using the PPBC electrolyte (Figure 6i). In clear contrast, the Li anode using the PPBB electrolyte presents a uniform and dense microstructure (Figure 6k). The corresponding atomic force microscopy (AFM) results also indicate that the surface roughness of the lithium foil using the PPBB electrolyte (280 nm) (Figure 6j) is lower than the PPBC electrolyte (332 nm) (Figure 6l). These results suggest that the PPBB electrolyte achieves uniform lithium stripping/plating and stable electrode/electrolyte interfacial.

© 2025 Wiley-VCH GmbH

15213773, 2025, 21, Downloaded from https://onlinelibrary.wiley.com/doi/10.1002/anie.202503037 by WUHAN UNIVERSITY OF TECHNOLOGY, Wiley Online Library on [05/09/2025]. See the Terms and Conditions (https://onlinelibrary.wiley.com/terms-and-conditions) on Wiley Online Library for rules of use; OA articles are governed by the applicable Creative Commons License

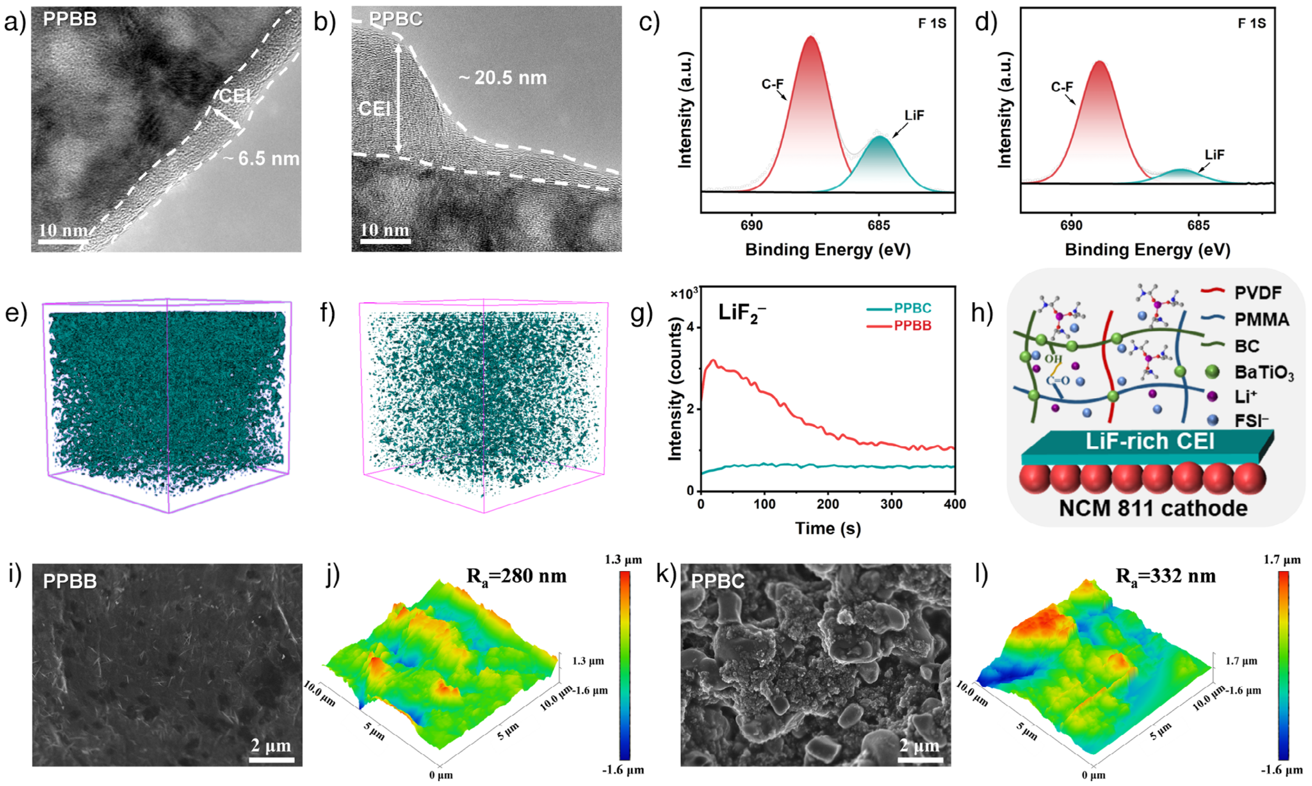

Figure 6. Characterization of the NCM811 full batteries after cycling. a)–b) High-resolution TEM images of NCM811 particles with various SPEs. The XPS spectra F 1 s of the CEI layer using c) PPBB electrolyte and d) PPBC electrolyte. ToF-SIMS 3D reconstruction of LiF_2^- on the CEI layer with e) PPBB electrolyte and f) PPBC electrolyte, and g) corresponding depth profiles. h) Illustration of cycled NCM811 cathode surface with PPBB electrolyte. SEM of Li anode surface with i) PPBB electrolyte and k) PPBC electrolyte. AFM morphology and corresponding surface roughness of Li anode using j) PPBB electrolyte and l) PPBC electrolyte.

Conclusion

In conclusion, we successfully adjust the Li^+ solvation structure and reduce the desolvation barrier in PVDF-based SPEs through an electric-dipole coupling ion–dipole engineering. The strong encapsulation ability of ion–dipole engineering, which inhibits the migration of free DMAC solvents and FSI^-, achieving wide voltage window and rapid Li^+ transfer. The electric-dipole engineering demonstrates strong Li salt dissociation and ion desolvation ability, resulting in increased mobile Li^+ concentration. Coupling the electric-dipole and ion–dipole engineering can obtain abundant Li^+ aggregates and inorganic-rich electrolyte/electrode interphases, resulting in excellent interfacial stability. As a result, the PPBB electrolyte displays a higher electrochemical window of 4.7 V and a higher t_{Li^+} of 0.62. The excellent electrochemical performances of solid-state NCM811|PPBB|Li and $LiFeO_4$|PPBB|Li cells demonstrate the exceptional compatibility of the PPBB electrolyte with high-voltage cathodes and lithium metal anodes. More importantly, the excellent cycling performance of both full cells paired with high-loading cathodes and pouch cells indicates their potential application prospects. In a nutshell, this study emphasizes the significance of adjusting the solvation-desolvation behavior in SPEs, which is critical for the commercialization applications of LMBs.

Acknowledgements

This work was supported by the National Key Research and Development Program of China (grant No. 2022YFB3803502), the National Natural Science Foundation of China (No. U23A20555), the National Energy-Saving and Low-Carbon Materials Production and Application Demonstration Platform Program (TC220H06N), the National Natural Science Foundation of China (No. 22409154), the Education Department of Hainan Province (Hnky2024ZD-26), and the Key Research and Development Program of Hubei (2022BAA027). We thank Chunyan Zhong from the Hainan Guangyu Biotechnology Co. for her guidance.

Conflict of Interests

The authors declare no conflict of interest.

Data Availability Statement

The data that support the findings of this study are available from the corresponding author upon reasonable request.

© 2025 Wiley-VCH GmbH

15213773, 2025, 21, Downloaded from https://onlinelibrary.wiley.com/doi/10.1002/anie.202503037 by WUHAN UNIVERSITY OF TECHNOLOGY, Wiley Online Library on [05/09/2025]. See the Terms and Conditions (https://onlinelibrary.wiley.com/terms-and-conditions) on Wiley Online Library for rules of use; OA articles are governed by the applicable Creative Commons License

Keywords: Electric-dipole • Ion-dipole • Residual Solvent • Solid-state Lithium Metal Batteries • Solvation-desolvation Behavior

---

[1] P. Prakash, B. Fall, J. Aguirre, L. A. Sonnenberg, P. R. Chinnam, S. Chereddy, D. A. Dikin, A. Venkatnathan, S. L. Wunder, M. J. Zdilla, *Nat. Mater.* **2023**, *22*, 627–635.
[2] Q.-K. Zhang, X.-Q. Zhang, J. Wan, N. Yao, T.-L. Song, J. Xie, L.-P. Hou, M.-Y. Zhou, X. Chen, B.-Q. Li, R. Wen, H.-J. Peng, Q. Zhang, J.-Q. Huang, *Nat. Energy* **2023**, *8*, 725–735.
[3] R. Chen, Q. Li, X. Yu, L. Chen, H. Li, *Chem. Rev.* **2020**, *120*, 6820–6877.
[4] D. Zhang, Y. Liu, S. Yang, J. Zhu, H. Hong, S. Li, Q. Xiong, Z. Huang, S. Wang, J. Liu, C. Zhi, *Adv. Mater.* **2024**, *36*, 2401549.
[5] J. Janek, W. G. Zeier, *Nat. Energy* **2016**, *1*, 16141.
[6] L.-Z. Fan, H. He, C.-W. Nan, *Nat. Rev. Mater.* **2021**, *6*, 1003–1019.
[7] S. Han, P. Wen, H. Wang, Y. Zhou, Y. Gu, L. Zhang, Y. Shao-Horn, X. Lin, M. Chen, *Nat. Mater.* **2023**, *22*, 1515–1522.
[8] P. Lennartz, B. A. Paren, A. Herzog-Arbeitman, X. C. Chen, J. A. Johnson, M. Winter, Y. Shao-Horn, G. Brunklaus, *Joule* **2023**, *7*, 1471–1495.
[9] X. Yu, L. Zhao, Y. Li, Y. Jin, D. J. Politis, H. Liu, H. Wang, M. Liu, Y.-B. He, L. Wang, *ACS Energy Lett.* **2024**, *9*, 2109–2115.
[10] L. Fan, S. Wei, S. Li, Q. Li, Y. Lu, *Adv. Energy Mater.* **2018**, *8*, 1702657.
[11] G.-R. Zhu, Q. Zhang, Q.-S. Liu, Q.-Y. Bai, Y.-Z. Quan, Y. Gao, G. Wu, Y.-Z. Wang, *Nat. Commun.* **2023**, *14*, 4617.
[12] Y. Meng, D. Zhou, R. Liu, Y. Tian, Y. Gao, Y. Wang, B. Sun, F. Kang, M. Armand, B. Li, G. Wang, D. Aurbach, *Nat. Energy* **2023**, *8*, 1023–1033.
[13] H. Xu, J. Yang, Y. Niu, X. Hou, Z. Sun, C. Jiang, Y. Xiao, C. He, S. Yang, B. Li, W. Chen, *Angew. Chem. Int. Ed.* **2024**, *63*, e202406637.
[14] P. Shi, J. Ma, M. Liu, S. Guo, Y. Huang, S. Wang, L. Zhang, L. Chen, K. Yang, X. Liu, Y. Li, X. An, D. Zhang, X. Cheng, Q. Li, W. Lv, G. Zhong, Y.-B. He, F. Kang, *Nat. Nanotechnol.* **2023**, *18*, 602–610.
[15] L. Zhu, J. Chen, Y. Wang, W. Feng, Y. Zhu, S. F. H. Lambregts, Y. Wu, C. Yang, E. R. H. van Eck, L. Peng, A. P. M. Kentgens, W. Tang, Y. Xia, *J. Am. Chem. Soc.* **2024**, *146*, 6591–6603.
[16] S. Zhang, H. Liu, Z. Liu, Y. Zhao, J. Yan, Y. Zhang, F. Liu, Q. Liu, C. Liu, G. Sun, Z. Wang, J. Yang, Y. Ren, *Adv. Funct. Mater.* **2024**, *34*, 2401377.
[17] Y. Yuan, Z. Zhang, Z. Zhang, K.-T. Bang, Y. Tian, Z. Dang, M. Gu, R. Wang, R. Tao, Y. Lu, Y. Wang, Y. Kim, *Angew. Chem. Int. Ed.* **2024**, *63*, e202402202.
[18] Y. Zeng, L. Zhao, J. Zhang, Q. Li, D. Sun, Y. Ren, Y. Tang, G. Jin, H. Wang, *Small Science* **2023**, *3*, 2300017.
[19] Q. Liu, G. Yang, X. Li, S. Zhang, R. Chen, X. Wang, Y. Gao, Z. Wang, L. Chen, *Energy Storage Mater.* **2022**, *51*, 443–452.
[20] Y. Zhu, Z. Lao, M. Zhang, T. Hou, X. Xiao, Z. Piao, G. Lu, Z. Han, R. Gao, L. Nie, X. Wu, Y. Song, C. Ji, J. Wang, G. Zhou, *Nat. Commun.* **2024**, *15*, 3914.
[21] K. Yang, J. Ma, Y. Li, J. Jiao, S. Jiao, X. An, G. Zhong, L. Chen, Y. Jiang, Y. Liu, D. Zhang, J. Mi, J. Biao, B. Li, X. Cheng, S. Guo, Y. Ma, W. Hu, S. Wu, J. Zheng, M. Liu, Y.-B. He, F. Kang, *J. Am. Chem. Soc.* **2024**, *146*, 11371–11381.
[22] W. Yang, Y. Liu, X. Sun, Z. He, P. He, H. Zhou, *Angew. Chem. Int. Ed.* **2024**, *63*, e202401428.
[23] K. Yang, L. Chen, J. Ma, C. Lai, Y. Huang, J. Mi, J. Biao, D. Zhang, P. Shi, H. Xia, G. Zhong, F. Kang, Y. B. He, *Angew. Chem. Int. Ed.* **2021**, *60*, 24668–24675.
[24] Q. Wu, M. Fang, S. Jiao, S. Li, S. Zhang, Z. Shen, S. Mao, J. Mao, J. Zhang, Y. Tan, K. Shen, J. Lv, W. Hu, Y. He, Y. Lu, *Nat. Commun.* **2023**, *14*, 6296.
[25] M. Li, H. An, Y. Song, Q. Liu, J. Wang, H. Huo, S. Lou, J. Wang, *J. Am. Chem. Soc.* **2023**, *145*, 25632–25642.
[26] P. Zhai, Z. Yang, Y. Wei, X. Guo, Y. Gong, *Adv. Energy Mater.* **2022**, *12*, 2200967.
[27] S. Xia, B. Yang, H. Zhang, J. Yang, W. Liu, S. Zheng, *Adv. Funct. Mater.* **2021**, *31*, 2101168.
[28] X. Zhang, S. Wang, C. Xue, C. Xin, Y. Lin, Y. Shen, L. Li, C.-W. Nan, *Adv. Mater.* **2019**, *31*, 1806082.
[29] C. Lai, C. Shu, W. Li, L. Wang, X. Wang, T. Zhang, X. Yin, I. Ahmad, M. Li, X. Tian, P. Yang, W. Tang, N. Miao, G. W. Zheng, *Nano Lett.* **2020**, *20*, 8273–8281.
[30] C. Xue, X. Zhang, S. Wang, L. Li, C.-W. Nan, *ACS Appl. Mater. Interfaces* **2020**, *12*, 24837–24844.
[31] B. Yang, C. Deng, N. Chen, F. Zhang, K. Hu, B. Gui, L. Zhao, F. Wu, R. Chen, *Adv. Mater.* **2024**, *36*, 2403078.
[32] L. Bi, L. He, Y. Song, Y. Wang, Q. Xie, P. Dong, Y. Zhang, Y. Yao, J. Liao, S. Wang, *Adv. Funct. Mater.* **2024**, *34*, 2311848.
[33] Y. Ye, X. Zhu, N. Meng, F. Lian, *Adv. Funct. Mater.* **2023**, *33*, 2307045.
[34] J. Xu, J. Chen, Y. Zhang, T. Liu, J. Fu, *Angew. Chem. Int. Ed.* **2021**, *60*, 7947–7955.
[35] G. Chen, F. Zhang, Z. Zhou, J. Li, Y. Tang, *Adv. Energy Mater.* **2018**, *8*, 1801219.
[36] Y. Li, Z. Sun, D. Liu, S. Lu, F. Li, G. Gao, M. Zhu, M. Li, Y. Zhang, H. Bu, Z. Jia, S. Ding, *Energy Environ. Mater.* **2021**, *4*, 434–443.
[37] M. A. S. Azizi Samir, L. Chazeau, F. Alloin, J. Y. Cavaillé, A. Dufresne, J. Y. Sanchez, *Electrochim. Acta* **2005**, *50*, 3897–3903.
[38] D. Zhang, Z. Luo, H. Xu, Y. Guo, H. Chen, Y. Ye, J. An, J. Hui, Y. Shi, S. Yang, B. Li, *Adv. Funct. Mater.* **2024**, *34*, 2409134.
[39] J. Kang, N. Deng, D. Shi, Y. Feng, Z. Wang, L. Gao, Y. Song, Y. Zhao, B. Cheng, G. Li, W. Kang, K. Zhang, *Adv. Funct. Mater.* **2023**, *33*, 2307263.
[40] Y. Ma, C. Wang, K. Yang, B. Li, Y. Li, S. Guo, J. Lv, X. An, M. Liu, Y.-B. He, F. Kang, *ACS Appl. Mater. Interfaces* **2023**, *15*, 17978–17985.
[41] L. Chen, T. Gu, J. Ma, K. Yang, P. Shi, J. Biao, J. Mi, M. Liu, W. Lv, Y.-B. He, *Nano Energy* **2022**, *100*, 107470.
[42] X. Ren, X. Zhang, Z. Shadike, L. Zou, H. Jia, X. Cao, M. H. Engelhard, B. E. Matthews, C. Wang, B. W. Arey, X.-Q. Yang, J. Liu, J.-G. Zhang, W. Xu, *Adv. Mater.* **2020**, *32*, 2004898.

Manuscript received: February 06, 2025
Revised manuscript received: March 14, 2025
Accepted manuscript online: March 14, 2025
Version of record online: March 24, 2025

© 2025 Wiley-VCH GmbH

15213773, 2025, 21, Downloaded from https://onlinelibrary.wiley.com/doi/10.1002/anie.202503037 by WUHAN UNIVERSITY OF TECHNOLOGY, Wiley Online Library on [05/09/2025]. See the Terms and Conditions (https://onlinelibrary.wiley.com/terms-and-conditions) on Wiley Online Library for rules of use; OA articles are governed by the applicable Creative Commons License